Signal to Noise Ratio and Spectral Sampling Constraints on Olivine Detection and Compositional Determination in the Intermediate Infrared Region: Applications in Planetary Sciences

S. A. Pérez-López[1], C. H. Kremer[2], and J. F. Mustard[1]

[1]Department of Earth, Environmental, and Planetary Sciences, Brown University, Providence, RI, USA, [2]Department of Geosciences, Stony Brook University, Long Island, NY, USA

Corresponding author: Sebastian Pérez-López (sebastian_perez-lopez@brown.edu)

Key Points:

- We use a feature fitting routine to predict olivine composition from degraded spectral data in the intermediate infrared region (4 – 8 μm).
- Accurate prediction of olivine composition is observed at data qualities expected of imaging spectrometers.

Abstract

The intermediate infrared region (IMIR, 4 – 8 μm) provides significant advantages over the visible-shortwave infrared and mid-infrared for quantitative determination of mafic mineral composition. In particular, olivine's sharp spectral features in IMIR spectra exhibit systematic shifts in wavelength position with iron-magnesium content. Previous IMIR studies have used laboratory data, with signal-to-noise ratios (SNRs) and spectral resolutions greater than those expected of imaging spectrometers. Here we employ a feature fitting algorithm to quantitatively assess the influence of SNR and sampling rate on olivine detection and compositional interpretation from IMIR data. We demonstrate that olivine is easily distinguished from pyroxene and other lunar-relevant minerals across IMIR wavelengths, with the feature-fitting algorithm effectively determining olivine composition for various synthetic, terrestrial, Martian, and lunar samples with an average error of only 6.4 mol%. We then apply the feature-fitting routine to degraded spectra with reduced SNRs and sampling rates, establishing data-quality thresholds for accurate determination of olivine composition. Spectra for the sample most relevant to lunar exploration, an Apollo 74002 drive tube consisting of microcrystalline olivine and glass-rich pyroclastics, required SNRs ≥ 200 for sampling rates ≤ 25 nm to predict composition within ±11 Mg# (molar Mg/[Mg+Fe] * 100) of the sample's true composition. Derived limits on SNRs and sampling rates will serve as valuable inputs for the development of IMIR imaging spectrometers, enabling comprehensive knowledge of olivine composition across the lunar surface and providing valuable insight into the Moon's crustal history and thermal evolution.

Plain Language Summary

An understanding of olivine composition can reveal the history of large-scale geologic processes. Here we explore olivine spectra in the intermediate infrared region (IMIR), where systematic trends in olivine's absorption bands are indicative of composition. We degrade laboratory olivine spectra to data qualities that are more realistic of imaging spectrometers used in planetary exploration and derive constraints on the signal-to-noise ratio and sampling rates required to accurately prediction olivine composition. These constraints will be useful in the development of IMIR imaging spectrometers.

1 Introduction

Olivine is an important rock forming mineral whose composition and early crystallization from silicate melts make it useful for discerning distinct crustal terranes and understanding the origin and evolution of magmatic sources. Geologically significant olivine-group minerals have compositions falling on the Fe-Mg solid-solution series, varying in Mg# (molar Mg/[Mg+Fe] * 100) between an Fe-rich endmember (fayalite, Mg# 0) and an Mg-rich endmember (forsterite, Mg# 100), with high-Mg compositions indicative of more primitive primary magmas. For the Moon and other planetary bodies, widespread characterization of olivine composition can provide insight into the planet's bulk thermal and chemical evolution.

Spectral features of olivine are known to exhibit consistent trends with Mg# and have been used to estimate olivine composition for certain locations on the Moon (e.g. Isaacson et al., 2011) and globally on Mars (e.g. Koeppen & Hamilton, 2008). To date, remote determination of olivine composition from spectroscopic data has been restricted to visible-near infrared (VNIR, 0.5 - 2

μm) and mid-infrared (MIR, 8 - 15 μm) wavelengths. In the VNIR, the position of three overlapping 1 μm bands arising from electronic transitions of Fe^{2+} are diagnostic of Mg# (e.g. Dyar et al., 2009) and can be inverted via the modified gaussian model (Sunshine et al., 1990) to ascertain composition (e.g. Clénet et al., 2011). In the MIR, restrahlen bands exhibit systematic shifts in band strength and linear trends in band position with changing cation ratios (Hamilton 2009, Lane 2011).

More recently, Kremer et al., 2020 demonstrated that the position of olivine overtone-combination bands at ~5.6 μm and ~6.0 μm exhibit systematic shifts to longer wavelengths with increasing Mg#, establishing applications for the intermediate infrared region (IMIR, 4 - 8 μm) in the remote determination of olivine composition. Additional advantages of IMIR spectroscopy include the capacity for remote determination of pyroxene composition (Kremer et al., 2023), as well as the presence of a 6.1 μm molecular water absorption and diminished effects from space weathering (Kremer et al., 2022).

To date, the IMIR region has been underutilized in the characterization of planetary surfaces due in part to previous engineering constraints that limited the viability of IMIR detectors as well as an array of strong atmospheric absorptions that preclude obtaining spectral information from the surface of bodies with non-negligible atmospheres. In addition, the IMIR region lies between the well-studied visible-short wavelength infrared region that relies primarily on solar radiation and the well studied mid-infrared wavelength region that relies primarly on emissivity. Currently the only hyperspectral instruments that cover IMIR wavelengths are the James Webb Space Telescope and the Stratospheric Observatory for Infrared Astronomy (SOFIA), an Earth-based airborne telescopic observatory operating at stratospheric altitudes (Stutzki 2006) that has ceased operations. SOFIA measurements of the lunar surface have been used to confirm the presence of molecular water on the Moon via the detection of a 6.1 μm fundamental H_2O absorption (Honniball et al., 2020), highlighting the potential of IMIR data in the surface characterization of airless bodies. Recent advances in engineering have resulted in infrared detectors capable of IMIR measurements (Ting et al., 2012, Cañas et al., 2020), positioning IMIR spectrometers as valuable tools for lunar exploration.

The relationship between band position and olivine chemistry in the IMIR region was established using laboratory data (Kremer et al., 2022), with spectral resolutions and signal-to-noise ratios (SNR) exceeding those expected of imaging spectrometers. The SNR of data acquired onboard spacecraft is known to decrease due to noise from electronic, optical, and thermal effects, and instrument limitations restrict sampling rates when compared to laboratory measurements. Variations in SNR and sampling rate may influence spectral interpretation by masking or modifying absorption features at low SNRs or poorly resolving absorption features at lower sampling rates (Swayze et al., 2003). In the case of remote determination of olivine composition from IMIR datasets, SNR and sampling rates will influence both the detection and compositional prediction of olivine.

Previous work that has studied the impact of data quality on spectral interpretation established limits for mineral identification in the VNIR using spectra that had been convolved to the band-passes and sampling intervals of various imaging spectrometers and further degraded with random noise (Swayze et al., 2003). The authors used Tetracorder's feature fitting algorithm

(Clark et al., 2003) to determine best-fit matches between degraded input spectra and an extensive spectral library that included a wide range of minerals and natural materials (Swayze et al., 2003). The motivation behind employing a feature fitting algorithm was twofold; it takes advantage of the full suite of spectral information within a given wavelength range and normalizes first-order differences in band strength and background absorption for a given spectral feature. This allows for direct comparison between spectra acquired under different optical conditions and with varying sample characteristics. To determine the relationship between band position and olivine composition in the IMIR region, Kremer et al. (2022) measured the band minima position of the two strongest absorption features at ~5.6 μm and ~6.0 μm. Additional features at ~4.9 μm, ~5.2 μm, and ~5.4 μm attributed to olivine were not used due to their weaker band strengths. In contrast, feature fitting makes use of the entire suite of spectral features, analyzing all absorption bands simultaneously to understand the influence of complete band shape on spectral interpretation.

Here we use a simplified feature fitting algorithm modeled after Tetracorder to determine the effects of SNR and sampling interval on the identification and compositional determination of olivine from IMIR spectra. Given the relevance of IMIR datasets to outstanding questions regarding lunar exploration, we build our spectral library around a variety of lunar-relevant minerals including a suite of synthetic olivine and pyroxene spectra of known compositions as well as spectra of anorthite, spinel, and ilmenite. We analyze feature fitting results from degraded spectra of olivine samples of known chemistry whose mineralogy and composition we predict from feature fitting against library spectra. These samples, which we refer to as 'test spectra' throughout, consist of 34 olivine samples of terrestrial, lunar, Martian, and synthetic origin. Library and test spectra are described further in Section 2.1. We explore a range of data qualities, degrading test spectra to SNRs of 50, 100, 150, 200, 300, 400, 500, and 600 and sampling rates of 10 nm, 15 nm, 20 nm, 25 nm, 30 nm, 40 nm, 50 nm, and 60 nm. Methods for noise superposition and downsampling are described in Section 2.2. Data quality constraints required for accurate olivine detection and compositional prediction derived from this study will feed forward into IMIR imaging spectrometer requirements.

2 Materials and Methods

2.1 Spectral Database

Spectra used in this study were acquired from the PDS Geosciences Node Spectral Library and the USGS Spectral Library. Spectra from the PDS Geosciences Node were measured at the NASA Reflectance Experiment Laboratory (RELAB) at Brown University using a Thermo-Nicolet Nexus 870 FTIR spectrometer (800 – 25,000 nm) and scaled to VNIR bidirectional reflectance spectra (300-2600 nm). Spectra compiled from the USGS Spectral Library were measured using either a Nicolet 740 FTIR or Magna-IR 762 FTIR and scaled to VNIR reflectance spectra measured with a Beckman 5270 spectrometer.

Sample and measurement properties for all spectra used in this study are listed in Tables 1 & 2, with spectra referred to by their sample # (TX for test spectra, LX for library spectra) or sample name throughout the study.

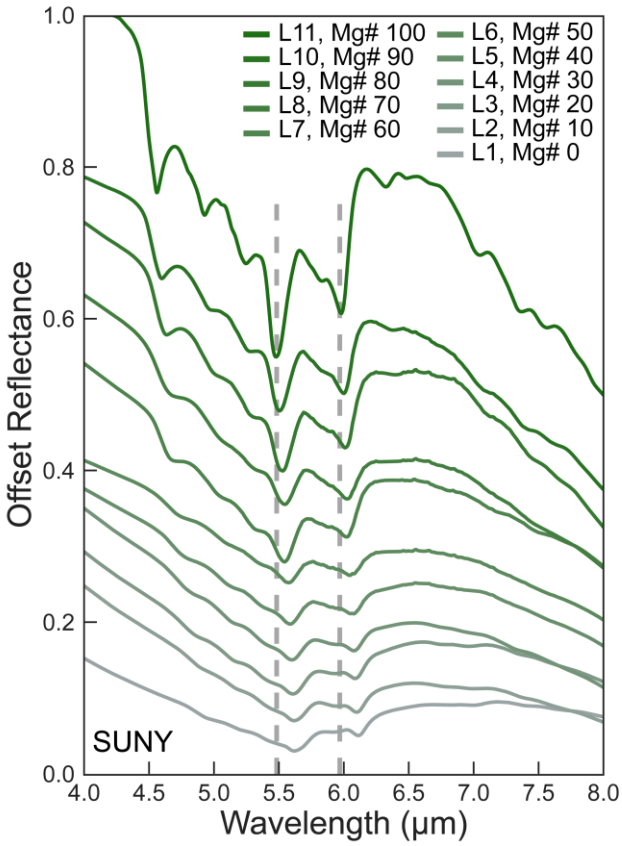

Figure 1. SUNY suite olivines. Note the trends in band position and muting of features with decreasing Mg#.

2.1.1 Library spectra

Our spectral library is composed of reflectance data of synthetic olivine of varying composition as well as a suite of lunar-relevant minerals including pyroxene, anorthite, spinel, and ilmenite. We include 11 spectra of synthetic olivine (SUNY suite) synthesized by Donald Lindsley and described in detail by Dyar et al., 2009. The suite consists of samples of high purity covering the complete Mg-Fe solid solution series. We include spectra of synthetic olivine at approximately 10 Mg# intervals ranging from 0 to 100 and decide to forego inclusion of synthetic samples with Mg#s 55, 65, and 75 to maintain a consistent interval between available library compositions across the entire solid-solution series (Fig. 1, Table 1). The synthetic SUNY sample with a composition between Mg# 80 and Mg# 100 falls slightly of the 10 Mg# interval with an Mg# of 89.5 instead of 90.

We also include a subset of spectra from a synthetic pyroxene suite synthesized by Donald Lindsley (Fig. S1). The full suite consists of 43 samples covering a range of pyroxene compositions spanning molar Ca content from 0 to 51 and Mg# from 0 to 100, and have been used in previous infrared studies of pyroxene (e.g. Klima et al., 2010, Kremer et al., 2023). To increase computational efficiency while still accounting for the influence of pyroxene composition on spectral features in the IMIR region (Kremer et al., 2023), we chose to include eight representative spectra from the larger 43-spectra dataset which covered endmember and

intermediate compositions across the pyroxene quadrilateral (Fig S1). Our spectral library also includes a spectrum of Miyake-jima anorthite with a Ca-composition (An# 98) comparable to that of the lunar anorthositic crust (e.g. Wood et al., 1970). We also provide endmember spectra (0.1 wt% FeO and 15.3 wt% FeO) from a suite of synthetic high-Mg spinel with lunar relevant compositions described in Jackson et al., 2014, as well as a spectrum of ilmenite separated from an Apollo 17 basalt. Library spectra are shown in Figs. 1 and 2 and sample characteristics and sources are listed in Table 1.

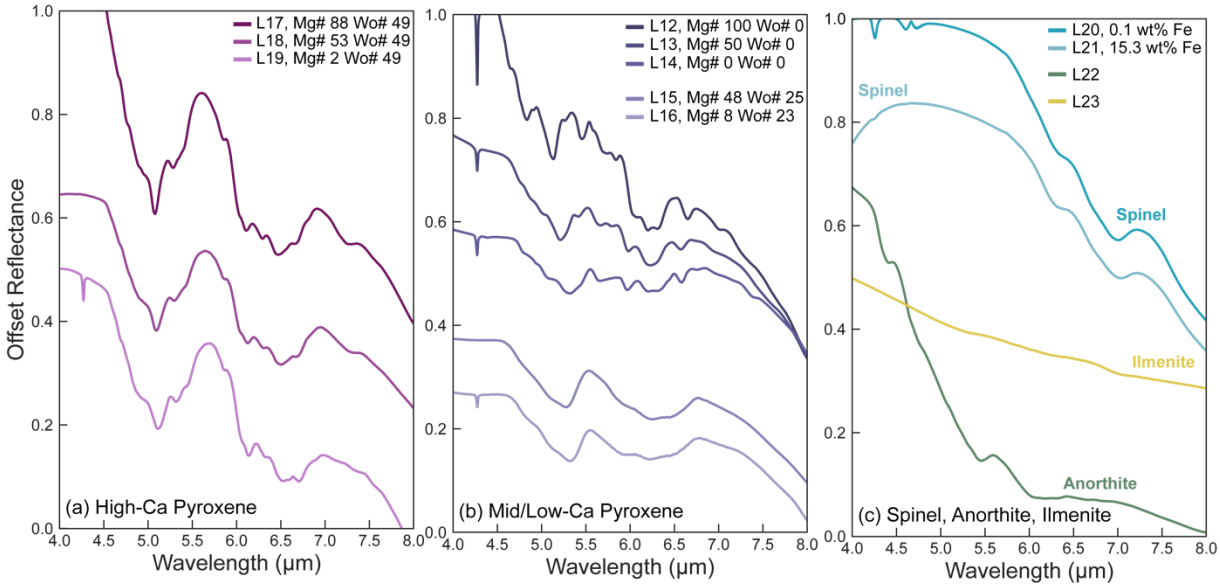

Figure 2. a) High-Ca synthetic pyroxenes covering the Mg-Fe solid-solution series. b) Mid and low-Ca synthetic pyroxenes covering the Mg-Fe solid solution series. c) Spinel, ilmenite, and anorthite. All spectra were acquired from RELAB and are described in Table 1.

Table 1. Library Spectra

Sample #	Mineral	Origin	Composition	Particle size (μm)	Native Sampling Rate	Sample Identifier (Source)
L1	Olivine	Synthetic (SUNY)	Mg# 0	<45	3 nm – 12 nm	DD-MDD-098 (RELAB)
L2	Olivine	Synthetic (SUNY)	Mg# 10	<45	3 nm – 12 nm	DD-MDD-097 (RELAB)
L3	Olivine	Synthetic (SUNY)	Mg# 20	<45	3 nm – 12 nm	DD-MDD-096 (RELAB)
L4	Olivine	Synthetic (SUNY)	Mg# 30	<45	3 nm – 12 nm	DD-MDD-095 (RELAB)
L5	Olivine	Synthetic (SUNY)	Mg# 40	<45	3 nm – 12 nm	DD-MDD-094 (RELAB)
L6	Olivine	Synthetic (SUNY)	Mg# 50	<45	3 nm – 12 nm	DD-MDD-093 (RELAB)
L7	Olivine	Synthetic (SUNY)	Mg# 60	<45	3 nm – 12 nm	DD-MDD-091 (RELAB)
L8	Olivine	Synthetic (SUNY)	Mg# 70	<45	3 nm – 12 nm	DD-MDD-089 (RELAB)

L9	Olivine	Synthetic (SUNY)	Mg# 80	<45	3 nm – 12 nm	DD-MDD-087 (RELAB)
L10	Olivine	Synthetic (SUNY)	Mg# 89.5	<45	3 nm – 12 nm	DD-MDD-086 (RELAB)
L11	Olivine	Synthetic (SUNY)	Mg# 100	<45	3 nm – 12 nm	DD-MDD-085 (RELAB)
L12	Pyroxene	Synthetic	Mg# 100 Wo 0	<45	3 nm – 12 nm	DL-CMP-001 (RELAB)
L13	Pyroxene	Synthetic	Mg# 50 Wo 0	<45	3 nm – 12 nm	DL-CMP-004 (RELAB)
L14	Pyroxene	Synthetic	Mg# 0 Wo 0	<45	3 nm – 12 nm	DL-CMP-061 (RELAB)
L15	Pyroxene	Synthetic	Mg# 48 Wo 25	<45	3 nm – 12 nm	DL-CMP-057 (RELAB)
L16	Pyroxene	Synthetic	Mg# 8 Wo2 3	<45	3 nm – 12 nm	DL-CMP-054 (RELAB)
L17	Pyroxene	Synthetic	Mg# 88 Wo 49	<45	3 nm – 12 nm	DL-CMP-043 (RELAB)
L18	Pyroxene	Synthetic	Mg# 53 Wo 49	<45	3 nm – 12 nm	DL-CMP-036 (RELAB)
L19	Pyroxene	Synthetic	Mg# 2 Wo 49	<45	3 nm – 12 nm	DL-CMP-082 (RELAB)
L20	Spinel	Synthetic	0.1 wt% FeO	<45	3 nm – 12 nm	SP-CMP-073-B (RELAB)
L21	Spinel	Synthetic	15.3 wt% FeO	<45	3 nm – 12 nm	SP-CMP-083-B (RELAB)
L22	Plagioclase	Miyake-jima	An# 98	45-75	3 nm – 12 nm	PL-CMP-151-C (RELAB)
L23	Ilmenite	Apollo 17	--	<45	3 nm – 12 nm	LR-CMP-222 (RELAB)

2.1.2 Test spectra

Test spectra consisted of reflectance data measured from a diverse range of synthetic, terrestrial, and extraterrestrial olivine with known compositions. These spectra were previously used to establish the relationship between band position and olivine chemistry in the IMIR region by Kremer er al., 2020. With the exception of the Apollo 74002 drive tube (T24-28), all test spectra were measured as particulate samples and consisted of pure olivine.

We include a second suite of synthetic olivine spectra (Bristol suite) which were synthesized by Richard Brooker and are described in Dyar et al., 2009 (Fig. 3a). We chose the SUNY suite as library spectra and the Bristol suite as test spectra based on the SUNY suite's greater chemical purity and comprehensive coverage of Mg# values at regular intervals. The Bristol suite, by contrast, had minor contamination of up to 18.7% Fe^{3+} and Mg# values ranging from 0 to 90 (Darby et al., 2009). Test spectra of terrestrial samples included olivine specimens from Dish Hill, California (Fig. 3b) and San Carlos, Arizona (Fig. 3c), as well as samples from the Kiglapait intrusion in Labrador, South Point, Hawaii, and Twin Sister Peak, Washington (Fig. 3d). Spectra of extraterrestrial samples included Martian meteorites Yamato 984028, Chassigny, NWA 2737, ALH 77005, and EETA 79001 (Fig. 3e). Lunar samples (Fig. 3f) included olivine extracted from a mare basalt (Apollo return sample 15555) as well as five spectra from different depths of the Apollo 74002 drive tube, a sample composed of ilmenite-rich pyroclastic beads hosting microscopic inclusions of olivine (Heiken & McKay, 1978).

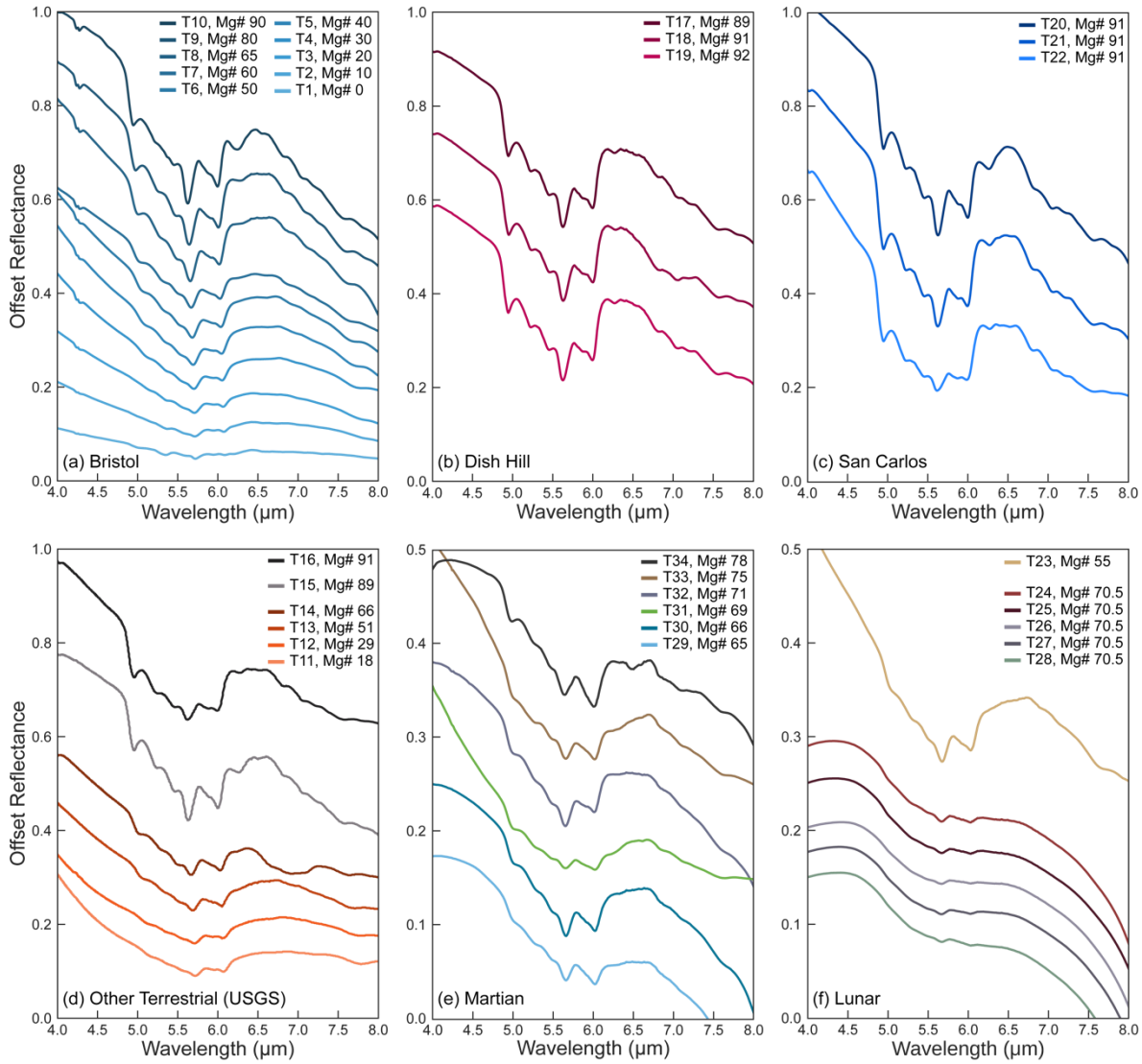

Figure 3. Test spectra included in this study. a) Synthetic Bristol suite. b) Dish Hill, California. c) San Carlos, Arizona. d) Twin Sister Peak, WA, South Point, HI, and Kiglapait intrusion. e) Martian meteorite samples NWA2737, EETA79001, ALH77005, Chassigny, Yamato-984028. f) Lunar samples 15555 separate and drive tube 74002. With the exception of the spectra in panel d which were acquired from the USGS spectral library, all spectra were acquired from RELAB and are described in Table 2.

Table 2. Test Spectra

Sample #	Sample Name	Origin	True Mg#	Predicted Mg#*	Particle size (μm)	Sampling Rate (nm)	Sample Identifier (Source)	IBD
T1	Bristol-046	Synthetic (Bristol)	0	20	<45	3 - 12	DD-MDD-046 (RELAB)	0.099
T2	Bristol-045	Synthetic (Bristol)	10	20	<45	3 - 12	DD-MDD-045 (RELAB)	0.101
T3	Bristol-044	Synthetic (Bristol)	20	20	<45	3 - 12	DD-MDD-044	0.113

							(RELAB)	
T4	Bristol-043	Synthetic (Bristol)	30	30	<45	3 - 12	DD-MDD-043 (RELAB)	0.146
T5	Bristol-042	Synthetic (Bristol)	40	30	<45	3 - 12	DD-MDD-042 (RELAB)	0.165
T6	Bristol-041	Synthetic (Bristol)	50	50	<45	3 - 12	DD-MDD-041 (RELAB)	0.161
T7	Bristol-040	Synthetic (Bristol)	60	70	<45	3 - 12	DD-MDD-040 (RELAB)	0.142
T8	Bristol-039	Synthetic (Bristol)	65	70	<45	3 - 12	DD-MDD-039 (RELAB)	0.181
T9	Bristol-038	Synthetic (Bristol)	80	80	<45	3 - 12	DD-MDD-038 (RELAB)	0.188
T10	Bristol-037	Synthetic (Bristol)	90	89.5	<45	3 - 12	DD-MDD-037 (RELAB)	0.202
T11	KI3377	Kiglapait	18	10	<60	10	KI3377 (USGS)	0.222
T12	KI3291	Kiglapait	29	10	<60	10	KI3291 (USGS)	0.213
T13	KI3188	Kiglapait	51	40	<60	10	KI3188 (USGS)	0.201
T14	KI3054	Kiglapait	66	60	<60	10	KI3054 (USGS)	0.190
T15	GDS70.d	South Point, HI	89	80	<60	10	GDS70.d (USGS)	0.226
T16	GDS71.b	Twin Sisters Peak, WA	91	89.5	<60	10	GDS71.b (USGS)	0.393
T17	DishHill-078	Dish Hill, CA	89	89.5	<45	3 - 12	DD-MDD-078 (RELAB)	0.226
T18	DishHill-076	Dish Hill, CA	91	89.5	<45	3 - 12	DD-MDD-076 (RELAB)	0.205
T19	DishHill-077	Dish Hill, CA	92	89.5	<45	3 - 12	DD-MDD-077 (RELAB)	0.201
T20	SanCarlos-080A	San Carlos, AZ	91	80	<63	3 - 12	PO-CMP-080A (RELAB)	0.247
T21	SanCarlos-080B	San Carlos, AZ	91	89.5	63-125	3 - 12	PO-CMP-080B (RELAB)	0.283
T22	SanCarlos-080C	San Carlos, AZ	91	100	125-250	3 - 12	PO-CMP-080C (RELAB)	0.415
T23	15555 Separate	Moon	55	70	<45	3 - 12	LR-CMP-212 (RELAB)	0.099
T24	74002.332	Moon	70.5	70	<500	3 - 12	LR-CMP-130 (RELAB)	0.063
T25	74002.2216	Moon	70.5	60	<501	3 - 12	LR-CMP-131 (RELAB)	0.072
T26	74002.2217	Moon	70.5	60	<502	3 - 12	LR-CMP-132 (RELAB)	0.065
T27	74002.2218	Moon	70.5	60	<503	3 - 12	LR-CMP-133 (RELAB)	0.081
T28	74002.2219	Moon	70.5	70	<504	3 - 12	LR-CMP-134 (RELAB)	0.084
T29	Y-984028-I	Mars	65	70	<45	3 - 12	DD-MDD-121	0.108

							(RELAB)	
T30	Y-984028-E	Mars	66	70	<45	3 - 12	DD-MDD-122 (RELAB)	0.138
T31	Chassigny	Mars	69	70	<50	3 - 12	DD-MDD-001 (RELAB)	0.343
T32	ALH77005	Mars	71	60	<50	3 - 12	DD-MDD-009 (RELAB)	0.166
T33	EETA79001	Mars	75	70	<50	3 - 12	DD-MDD-060 (RELAB)	0.268
T34	NWA2737	Mars	78	70	<45	3 - 12	DD-AHT-065 (RELAB)	0.170

*Mg# predicted from feature fitting on laboratory-quality data

2.2 Spectral Degradation:

We explore the influence of noise and spectral resolution on spectral interpretation by degrading test spectra to a range of SNRs and sampling rates. For a given round of feature fitting, the test spectrum and library spectra were resampled to a given sampling rate (Section 2.2.1) and further degraded with the superposition of noise (Section 2.2.2). Degraded test spectra were then subjected to a feature fitting algorithm and compared against library spectra (Section 2.3), with best-fit library matches recorded and used to evaluate the impact of noise and sampling on spectral interpretation.

2.2.1 Resampling

To explore the effect of sampling rate on spectral interpretation, Swayze et al., 2003 used band pass and sampling interval information from four imaging spectrometers (AVIRIS, HYDICE, MIVIS, and VIMS) to reproduce the spectrometer's spectral resolution. Here we focus on a simple downsampling of the laboratory data by calculating resampled reflectance values as a weighted sum of the fraction of reflectance values in the original wavelength domain that fall under the resampled wavelength domain. We resample test spectra before the superposition of noise.

We limit our resampling to uniform sampling intervals beginning at 4 μm and resample spectra to intervals of 10 nm, 15 nm, 20 nm, 25 nm, 30 nm, 40 nm, 50 nm, and 60 nm. Sampling rates for laboratory spectra acquired from the USGS and RELAB databases were 10 nm and 3 nm – 12 nm across IMIR wavelengths, respectively.

2.2.2 Noise

Increasing levels of scaled gaussian noise were superimposed on test spectra uniformly across all wavelengths. Noise spectra were randomly sampled from a normal distribution with a mean of zero and a set standard deviation. Following Swayze et al., 2003, we define SNR for a surface of 50% reflectance, where a reflectance level of 0.5 is divided by the standard deviation of the noise spectrum.

Each noise spectrum defined by an SNR represets a random draw from the given distribution, with individual outcomes varying. To ensure statistical precision for each round of feature fitting we downsampled and degraded all test spectra to the lowest data qualities explored in this study (SNR 50, sampling rate 60 nm) and calculated the variance in olivine detection rates and average Mg# prediction across an increasing number of runs. After ~1500 runs, variations in olivine

detection rates were well within ± 2.5% and variations in average Mg# prediction were well within ± 2.5 Mg#, with minimal increases in precision observed over a greater number of runs (Fig. 4). For each round of feature fitting we degrade test spectra to a given sampling rate and SNR for 3000 rounds. For each iteration, the test spectrum is degraded via the superposition of a new noise spectrum which is randomly sampled from the gaussian distribution defined by that round's SNR.

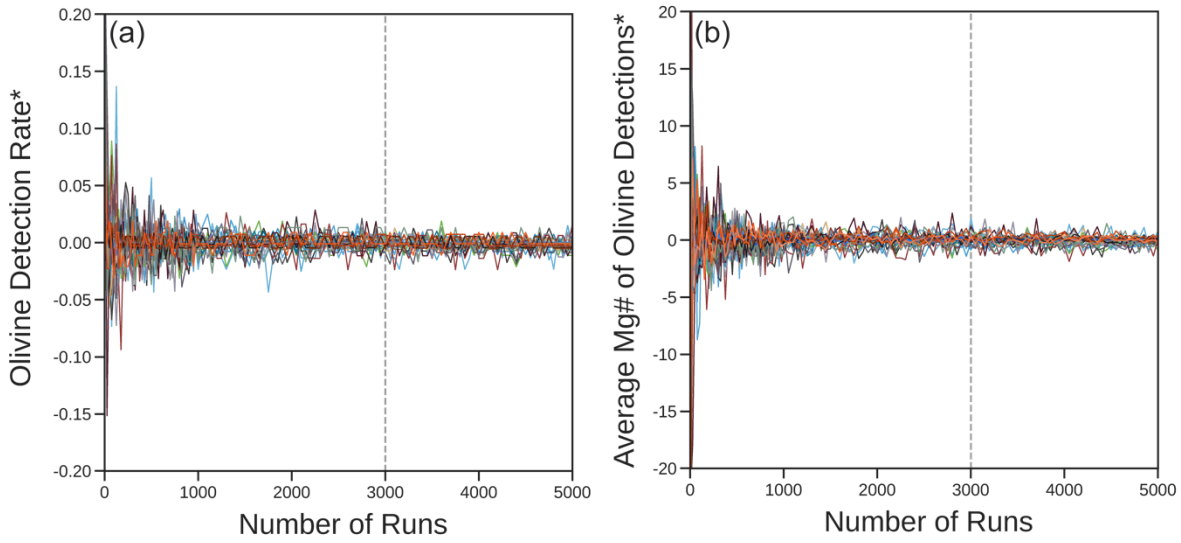

Figure. 4 a) Olivine detection rate and b) average Mg# of olivine detections for all test spectra across an increasing number of runs. *Data has been demeaned for clarity. Raw data is shown in Fig. S2.

We degrade spectra to SNRs of 50, 100, 150, 200, 300, 400, 500, and 600. Our choice to define SNR relative to a surface of 50% reflectance allows us to standardize discussion of SNR throughout the work, however equivalent SNRs will have different relative effects on test spectra depending on the samples spectral contrast. To place SNR in context with the test spectrum's spectral contrast, we calculate integrated band depths (IBDs) following Milliken & Mustard, 2005 (eq. 1), where R(λ) represents the reflectance value of the absorption, $R_c(\lambda)$ represents the reflectance value of the continuum, and $d\lambda$ is the sampling interval. IBD values serve as an approximation of the cumulative energy represented by all absorptions occurring within the integrated spectral range (Milliken & Mustard, 2005). For uniformity, all test spectra were resampled to 10 nm for the IBD calculations listed in Table 2.

$$IBD = \frac{\int_{\lambda_{min}}^{\lambda_{max}} 1-\frac{R(\lambda)}{R_C(\lambda)} * d\lambda}{\lambda_{max}-\lambda_{min}} \quad (1)$$

An example of degraded test spectra across the range of SNRs and sampling rates explored in this study are shown in Fig. 5.

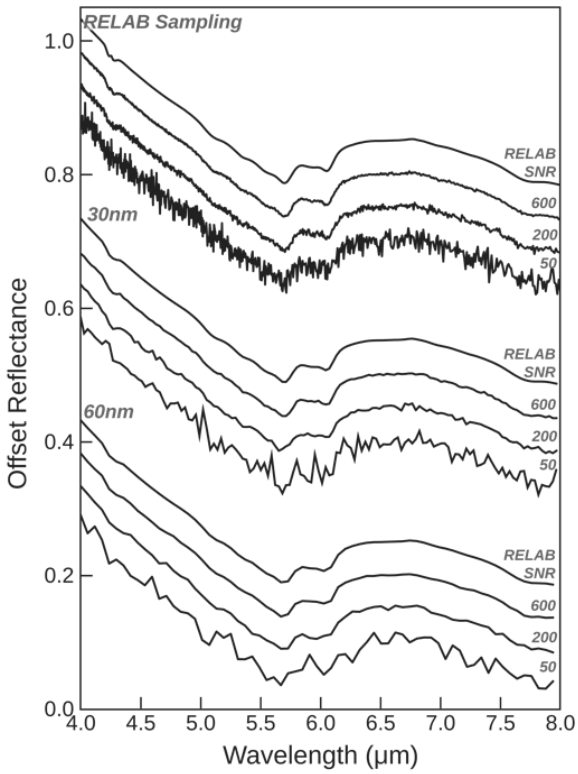

Figure 5. Bristol Mg# 30 spectra degraded to various combination of SNR and sampling rate explored in this study. RELAB sampling rates range from 3 nm – 12 nm across IMIR wavelengths.

2.3 Feature Fitting:

We calculate best-fit matches between artificially degraded olivine spectra of known composition and a spectral library of lunar-relevant minerals as described in Section 2.1.1. Test spectra consisted of synthetic and natural olivine samples as described in Section 2.1.2.

For a single round of feature fitting, we start by isolating the spectral feature of interest by removing a continuum defined by the spectra's convex-hull (Fig. 6b). The feature fitting routine requires that a continuum be removed using a set of fixed channels bounding the feature of interest. We determine band positions for the continuum boundaries from the convex hull of the SUNY Mg#100 library spectrum since high-Mg olivine endmembers exhibit the strongest spectral features in this wavelength range. The resulting continuum bounds were found to be 4.69 μm and 6.56 μm on the original wavelength domain. In rounds where spectra were resampled, the bands closest to those values were selected.

In the IMIR region, smaller particle sizes result in greater spectral contrast (e.g. Fig. 3c, T20-T22). We account for the first order effects of grain size and band saturation via a linear gain and offset measurement (Clark et al., 2003). The linear gain and offset adjustment serves to normalize spectral contrast between the test spectrum and library spectra and its simplicity

enables rapid digestion of large spectral datasets (Fig. 6c). An adjusted library spectrum is calculated by using an additive constant, k

$$R'(\lambda) = \frac{R_{CR}(\lambda) + k}{1.0 + k} \qquad (2)$$

where R_{CR} represents the continuum-removed library reflectance values. The linear form of eq. 2 can be written as follows:

$$R' = \frac{k}{1.0 + k} + \frac{1.0}{1.0 + k} R_{CR} \qquad (3)$$

A standard linear least-squares regression is then used to determine the optimal k value to fit the adjusted library spectrum to the degraded test spectrum.

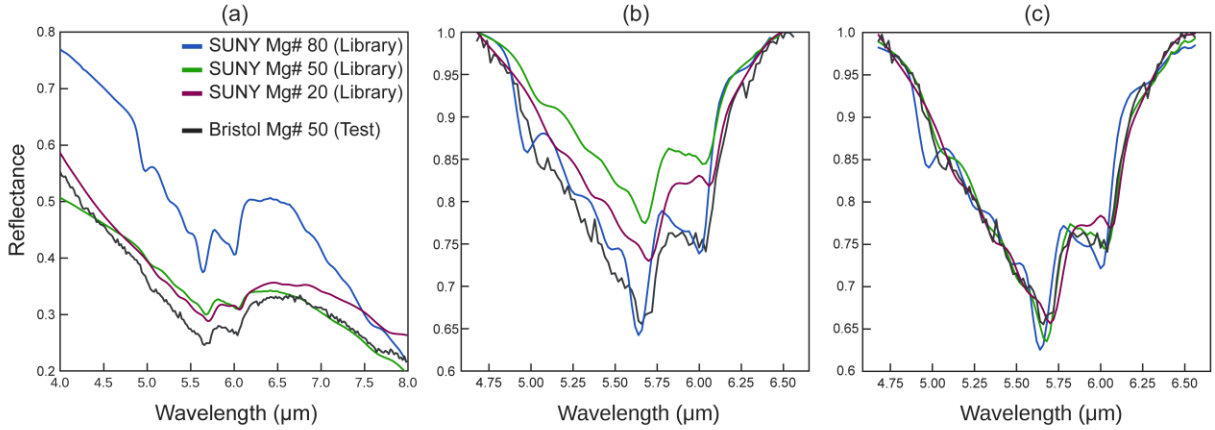

Figure 6. Simplified example of a feature fitting routine with degraded Bristol-041 spectrum (200 SNR, 20 nm sampling) and three library spectra, SUNY Mg# 20, 50, and 80. a) Laboratory reflectance data of degraded test and library samples. b) Continuum-removed reflectance. c) Library spectra fit to degraded Bristol spectra following a linear-gain and offset adjustment.

The library spectrum that provides the best overall fit is determined by calculating the Root Mean Square Error (RMSE) between the continuum-removed test spectrum and each optimized library spectra (Fig. 7). Each round serves as a unique spectral interpretation with the best-fit library spectra taken as a mineral detection. We refrain from specifying an RMSE threshold required for identification since there was no value that would serve to minimize the number of false detections while not concurrently negating a large number of true detections. In this regard, this study serves to identify upper limits on SNRs and sampling rates required for olivine detection and accurate interpretation of olivine chemistry from IMIR data.

Because the composition of all the olivine samples included as both test and library spectra are known, in rounds where olivine was detected the composition of the best-fit library spectra was further considered as an Mg# prediction for the degraded test spectra (Fig. 7). Identification rates were then calculated for test spectra degraded to various data qualities.

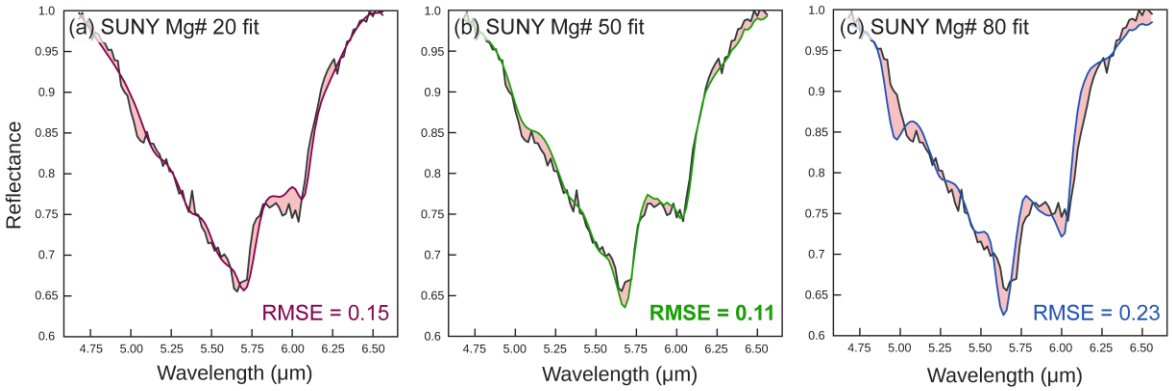

Figure. 7 RMSE calculation of three library spectra after feature fitting a) SUNY Mg#20, b) SUNY Mg# 50, c) SUNY Mg# 80. Here, SUNY Mg#50 had the lowest RMSE and is considered the best-fit mineral and subsequent Mg# prediction for the degraded Bristol-048 spectrum whose true Mg# is 50.

3 Results

3.1 Olivine Identification Rates

For each round of feature fitting we consider the best-fit library spectra as a mineral detection regardless of composition. For all test spectra degraded to any combination of SNR and sampling rate, olivine was the predominant mineral detection across a set of feature fitting runs. The parameter space required to achieve 100% olivine detection across all test spectra are shown in Fig. S3.

With the exception of Chassigny, test spectra with high spectral contrast were correctly identified as olivine over all feature fitting runs across all combinations of SNR and sampling rates explored (Fig. S3). Notably, the Chassigny test spectrum, which had a relatively large IBD of 0.343, was falsely identified as anorthite up to 15% of the time when degraded to the lowest data qualities. While olivine detections dominated regardless of test spectrum or data quality, for samples with lower IBDs (e.g. low-Mg synthetic samples (T1-2), lunar samples (T23-28), and sample Y-984928-I (T29)), test spectra degraded to low-SNRs and high-sampling rates would occasionally be falsely-identified as ilmenite or anorthite, with minimal false detections of spinel or pyroxene. Across the over 6.5 million feature fitting runs covering all SNRs, sampling rates, and test spectra explored here, pyroxene was falsely detected only 540 times. False detections of ilmenite and anorthite were confined to SNRs $\leq$150 and accounted for only 0.30% and 0.20% of all detections, respectively.

The sample that required the finest data qualities (highest SNRs and finest sampling rates) to reach 100% olivine detection was the Apollo drive tube sample 74002.332 (T24 – 28). In order to achieve 100% olivine detection for this sample, spectra had to have an SNR of 100 for a sampling rate of 10 nm, SNRs $\geq$ 150 for sampling rates under 30 nm, and SNRs $\geq$ 200 for sampling rates of 40 - 60 nm.

3.2 Compositional Prediction of Olivine Using Feature Fitting on Laboratory-Quality Data

We first investigate the accuracy of our feature fitting routine on compositional determination of laboratory-quality data. Across the 34 test spectra, the average absolute error in Mg# prediction was 6.39 mol%, reinforcing the utility of IMIR wavelengths in the determination of olivine composition as well as the application of our feature fitting routine for compositional prediction. 35% of test spectra (12 out of 34 samples) were predicted within ± 2 Mg# of their true compositions, 91% of test spectra (31 out of 34 samples) were predicted to be within ± 11 Mg# of their true compositions, and the remaining three test spectra were predicted to be within ± 20 Mg# of their true compositions (Fig. 8).

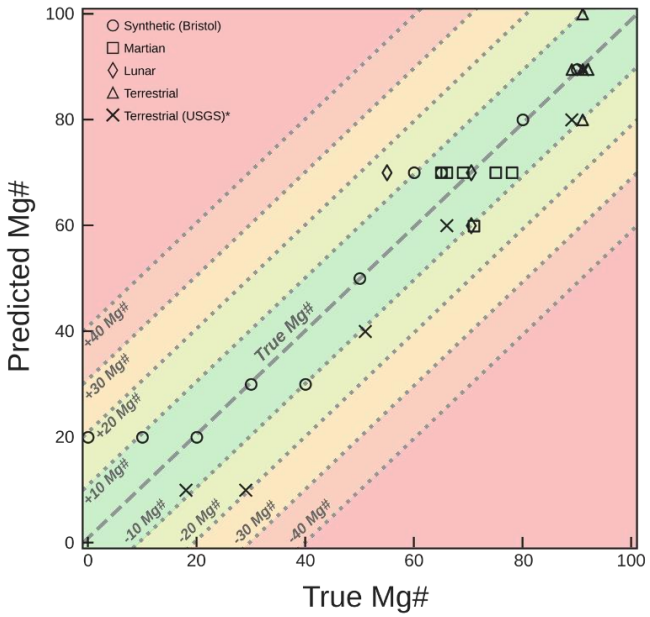

Figure 8. Undegraded test spectra true Mg# plotted against Mg# prediction from feature fitting. *For USGS samples, all spectra were resampled to 10 nm since test spectra and library spectra had different native sampling domains.

3.3 Effects of SNR and Sampling Rate on Olivine Mg# Interpretation

We then study the effects of spectral degradation on compositional interpretation for the 31 test spectra predicted within ±11 Mg# of their true composition on laboratory quality data. We forego analysis of Bristol-046 (T1), KI3291 (T12), and the 15555 Separate (T23) since their compositional predictions fell outside of this range (Section 3.2).

Significant variations in the accuracy of compositional predictions were observed among test spectra that had been degraded to a given SNR and sampling rate. The Dish Hill (T17 -19), San Carlos (T20 – 22), Bristol-038 (T9), GDS71.b (T16) samples, all of which displayed well-defined absorptions with high IBDs, were predicted within ±11 Mg# of their true composition across all runs for the data qualities explored here (Fig. S4). Nine other samples (T5, T7, T8, T13. T14, T20, T32, T33) were predicted within ±11 Mg# of their true composition for ≥ 90% of runs for SNRs ≥ 50. The lunar drive tube samples (T24 – 28) required SNRs greater than 200 to achieve ≥ 90% compositional prediction within ±11 Mg# for the sampling intervals explored here (Fig. 9).

The only test spectrum that did not reach ≥ 90% compositional prediction within ±11 Mg# across the parameter space explored here was Y-984028-E (T30), which has an Mg# of 66 and was predicted as Mg# 70 on laboratory quality data using the feature fitting routine. At high SNRs (≥ 400) and low sampling rates (≤ 20 nm), best-fit predictions for Y-984028-E oscillated between Mg# 70 and Mg# 50. At the least-degraded data quality (SNR 600 and sampling rate of 10 nm), ~76% of best-fit library matches were Mg# 70 (4 mol% from true value), while the remaining detections interpreted the composition as Mg# 50 (16 mol% from true value).

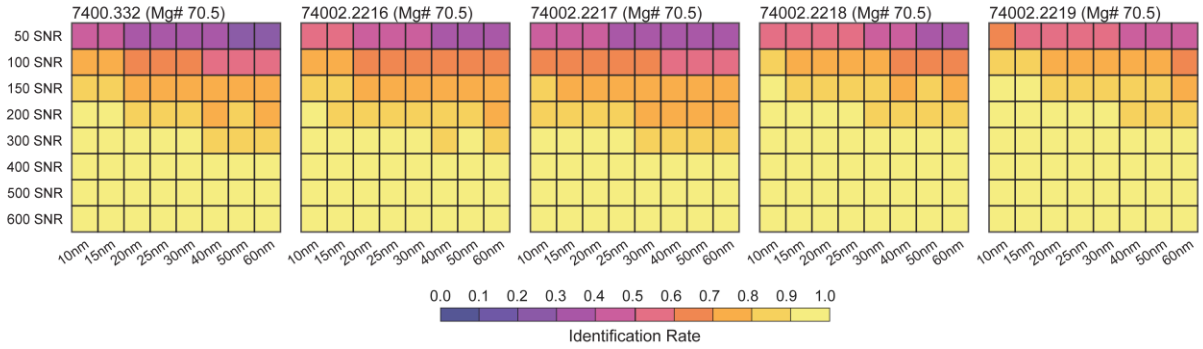

Figure. 9 Identification rates within ±11 Mg# of test spectrum's true composition. Each grid space represents the result of 3000 feature fits, with each iteration generating a new degraded test spectra from randomly sampled noise defined by that grid's SNR and resampled to the grid's sampling rate.

4 Discussion

4.1 Olivine Detection in the IMIR Region

In the VNIR, olivine interpretation is complicated both by the fact that olivine has 3 overlapping features at 1 µm and by the fact that the 3-band composite feature overlaps with a broad 0.9 µm pyroxene absorption arising from electronic transitions. In contrast, in the IMIR region, olivine absorptions are the result of multiple, discrete overtone-combination bands (Kremer et al., 2020). The spectral complexity results in readily distinguishable spectral signatures for olivine when compared to pyroxene and other lunar-relevant minerals across IMIR wavelengths (e.g. Figs. 1 & 2). For the test spectra explored here, olivine was by far the most common best-fit library mineral for a given set of feature fitting runs when compared to pyroxene, anorthite, spinel, and ilmenite.

4.2 Successful Compositional Prediction via Feature Fitting

The low absolute error in Mg# prediction across laboratory-quality data strengthens the validity of utilizing IMIR wavelengths for remote determination of olivine composition and emphasizes the practicality of employing a feature fitting approach for predictive compositional analysis.

The synthetic olivine suite included in our spectral library was limited to samples covering the solid-solution series at intervals of roughly 10 Mg#. Prediction accuracy for a given round of feature fitting is constrained by the available olivine compositions in the spectral library (e.g. a test spectra of known Mg# 65 could at best be predicted with an error of 5 mol%, as either Mg# 60 or Mg# 70). Accuracy of the feature fitting routine is thus directly tied to the spectral library, and can be improved upon with synthetic suites that cover the solid-solution series at finer

intervals, or expanded upon for other applications, for example with library spectra of lunar-relevant mixtures. This is in contrast to the band-minima technique employed by Kremer et al., 2020, where the prediction accuracy is limited instead by spectral resolution and can be strongly effected by SNR. For a sampling rate of just 20 nm, the resolution in Mg# prediction using the band minima equations derived by Kremer et al., 2020 would be ~17 Mg# for the 5.6 μm band and ~19 Mg# for the 6 μm band.

4.3 Effects of Degradation on Compositional Prediction

Mineral detection requires sufficient spectral contrast to detect absorption features diagnostic of a mineral's crystal structure. With regards to remote determination of olivine Mg# from degraded IMIR spectra, spectral contrast will influence the degradation thresholds required for accurate mineral detection as well as any subsequent compositional predictions. Since we define our SNR relative to a surface of 50% reflectance, test spectra with smaller IBDs generally required higher SNRs before reaching a given identification threshold.

4.3.1 Insights From Synthetic Samples

The Bristol suite highlights a general trend in both increasing olivine detection rates and increasing accuracy of compositional interpretation with increasing Mg#. In the IMIR region, absorption strengths increase with magnesium concentration. Consequently, targets with higher Mg# exhibit increased spectral contrast, making them favorable for detection and compositional analysis. This carries significant implications for the exploration of Mercury, whose surface lacks significant amounts of ferrous iron resulting in an absence of detectable spectral features in VNIR data (McCord & Clark 1979, Nittler et al., 2011). The Mg# of returned lunar samples has been relatively high, with ferroan anorthosites and alkali-suite samples falling in the range of ~30 to ~70 Mg# and Mg-suite samples having Mg#s greater than ~60 (Shearer et al., 2015).

4.3.2 Insights From Natural Samples

The variability in identification rates across terrestrial, Martian, and lunar test spectra reveals the numerous factors that play a role in spectral interpretation when examining natural samples. Band strengths and band shapes will vary with olivine composition, grain size, and mineral abundance in mixtures. Spectral shape and spectral contrast will further be influenced by the presence of alteration products, chemical impurities and minor cation substitutions, and, for lunar samples, space weathering effects.

A strength of the band-minima approach employed by Kremer et al., 2020 is that compositional prediction relies solely on the band minima position of the ~5.6 μm and ~6.0 μm bands and is therefore less impacted by overall band shape. While the feature fitting routine normalizes first-order differences in band strength via a linear scaling routine, the various physical and chemical parameters affecting band strength will also influence the overall spectral shape and subsequent mineralogic and compositonal interpretations.

An example can be seen in the three San Carlos samples (T20 – T22), which were identical in composition (Mg #91) and sample characteristics besides grain size. Reflectance measurements are highly grain size dependent as grain size dictates the internal path length traveled by photons and the proportions of the photons that are absorbed versus scattered (Clark & Roush 1984, Clark 1999). The three San Carlos samples were estimated to have Mg#s of 80, 89.5 and 100 on

undegraded data using the feature fitting routine for grain sizes of <63 µm, 63 – 125 µm, and 125 – 250 µm, respectively. While all three estimations, regardless of grain size, fell within ±11 Mg# of the sample's true composition, it demonstrates how feature fitting accuracy is dependent on all factors controlling the overall spectral shape, of which composition is only one.

4.3.3 Olivine Separates and Bulk Measurements

Of the 34 test spectra used in this study, 30 were olivine samples which had been separated from their original matrix. In the context of planetary exploration, a given pixel measured by an imaging spectrometer will almost certainly represent a mixture of materials in contact as either regolith or rock. The resulting spectra will be a non-linear combination of the end-member components of the mixture, which will affect the overall band shape and may influence compositional predictions via the feature fitting routine. Four test spectra acquired from the Apollo 74002 drive tube (T25-28) were measured as bulk samples of ilmenite-rich pyroclastic samples comprising of glass-rich beads containing microcrystalline olivine (Heiken & McKay, 1978). All four of these test spectra were predicted within ±11 Mg# of their true composition via feature fitting on laboratory-quality data. When degraded, the samples had similar identification rates for a given SNR and sampling intervals, requiring SNRs ≥ 200 for sampling rates ≤ 25 nm and SNRs ≥ 300 for sampling rates between 30 nm and 60nm to reach >90% identification within ±11 Mg#. These results suggest that compositional predictions derived from feature fitting of IMIR data are accurate for lunar regolith and pyroclastic targets.

5 Conclusions

We investigate the utility of feature fitting on IMIR data for the remote determination of olivine composition and quantitatively identify SNR and sampling rate thresholds required for accurate remote determination of olivine Mg#. We show that:

1. Olivine absorptions in the IMIR range are easily distinguishable from other lunar-relevant minerals, with 100% of runs detected as olivine across all test spectra for SNRs ≥ 150 and sampling rates ≤ 30 nm.

2. Comparison of complete band shape via feature fitting is effective at predicting olivine composition using laboratory IMIR data for synthetic, terrestrial, Martian, and lunar samples, with an overall absolute error in compositional prediction of 6.39 Mg# across all test spectra and 91% of test spectra predicted with ±11 Mg# of their true composition.

3. Applications with more idealized measurements (e.g. minimized spectral mixing over a given pixel; rover/lander spectrometer, laboratory studies) have more lenient data constraints, with some test spectra detected within ±11 Mg# for 100% of their true compositions across all runs, despite being degraded to the worst data qualities (30 SNR, 60 nm sampling).

4. SNRs ≥ 200 for sampling rates ≤ 25 nm and SNRs ≥ 300 for larger sampling rates are optimal to accurately estimate the composition of a lunar drive tube sample of ilmenite and glass-rich beads within ±11 Mg# of their true composition across ≥ 90% of runs.

Acknowledgments

This work was supported in part by the National Science Foundation Graduate Research Fellowship under Grant No. 2040433 (S.P.L) and the NASA Postdoctoral Program (C.K.) We thank Michael Bramble for valuable discussion throughout the work.

Data Availability

The data used in this study as well as code files for feature fitting may be accessed at https://doi.org/10.5281/zenodo.10368444 (Pérez-López et al., 2023).

References

Burns, R. G. (1970). Crystal field spectra and evidence of cation ordering in olivine minerals. *American Mineralogist, 55,* 1608-1632.

Cañas, C., Pagano, T. S., & Rafol, S. B. (2020). Radiometric performance characterization of the CubeSat Infrared Atmospheric Sounder (CIRAS) High Operating Temperature-Barrier Infrared Detectors (HOT-BIRD). In C. D. Norton, T. S. Pagano, & S. R. Babu (Eds.), *CubeSats and SmallSats for Remote Sensing IV* (p. 6). Online Only, United States: SPIE. https://doi.org/10.1117/12.2570533

Clark, R.N. (1999). Spectroscopy of Rocks and Minerals, and Principles of Spectroscopy. Manual of Remote Sensing, 3rd. ed.

Clark, R. N., & Roush, T. L. (1984). Reflectance spectroscopy: Quantitative analysis techniques for remote sensing applications. *Journal of Geophysical Research: Solid Earth*, *89*(B7), 6329–6340. https://doi.org/10.1029/JB089iB07p06329

Clark, R. N., Swayze, G. A., Livo, K. E., Kokaly, R. F., Sutley, S. J., Dalton, J. B., et al. (2003). Imaging spectroscopy: Earth and planetary remote sensing with the USGS Tetracorder and expert systems. *Journal of Geophysical Research: Planets*, *108*(E12), 2002JE001847. https://doi.org/10.1029/2002JE001847

Clénet, H., Pinet, P., Daydou, Y., Heuripeau, F., Rosemberg, C., Baratoux, D., & Chevrel, S. (2011). A new systematic approach using the Modified Gaussian Model: Insight for the characterization of chemical composition of olivines, pyroxenes and olivine–pyroxene mixtures. *Icarus*, *213*(1), 404–422. https://doi.org/10.1016/j.icarus.2011.03.002

Dyar, M. D., Sklute, E. C., Menzies, O. N., Bland, P. A., Lindsley, D., Glotch, T., et al. (2009). Spectroscopic characteristics of synthetic olivine: An integrated multi-wavelength and multi-

technique approach. *American Mineralogist*, *94*(7), 883–898. https://doi.org/10.2138/am.2009.3115

Hamilton, V. E. (2010). Thermal infrared (vibrational) spectroscopy of Mg–Fe olivines: A review and applications to determining the composition of planetary surfaces. *Geochemistry*, *70*(1), 7–33. https://doi.org/10.1016/j.chemer.2009.12.005

Heiken, G., & McKay, D. (1978). Petrology of a sequence of pyroclastic rocks from the valley of Taurus-Littrow (Apollo 17 landing site). *Lunar and Planetary Science Conference Proceedings*, *2*, 1933–1943. Retrieved from https://ui.adsabs.harvard.edu/abs/1978LPSC....9.1933H

Honniball, C. I., Lucey, P. G., Li, S., Shenoy, S., Orlando, T. M., Hibbitts, C. A., et al. (2020). Molecular water detected on the sunlit Moon by SOFIA. *Nature Astronomy*, *5*(2), 121–127. https://doi.org/10.1038/s41550-020-01222-x

Isaacson, P. J., Pieters, C. M., Besse, S., Clark, R. N., Head, J. W., Klima, R. L., et al. (2011). Remote compositional analysis of lunar olivine-rich lithologies with Moon Mineralogy Mapper (M^3) spectra. *Journal of Geophysical Research*, *116*, E00G11. https://doi.org/10.1029/2010JE003731

Jackson, C. R. M., Cheek, L. C., Williams, K. B., Hanna, K. D., Pieters, C. M., Parman, S. W., et al. (2014). Visible-infrared spectral properties of iron-bearing aluminate spinel under lunar-like redox conditions. *American Mineralogist, 99*(10), 1821–1833. https://doi.org/10.2138/am-2014-4793

Klima, R. L., Pieters, C. M., & Dyar, M. D. (2007). Spectroscopy of synthetic Mg-Fe pyroxenes I: Spin-allowed and spin-forbidden crystal field bands in the visible and near-infrared. *Meteoritics & Planetary Science*, *42*(2), 235–253. https://doi.org/10.1111/j.1945-5100.2007.tb00230.x

Koeppen, W. C., & Hamilton, V. E. (2008). Global distribution, composition, and abundance of olivine on the surface of Mars from thermal infrared data. *Journal of Geophysical Research: Planets*, *113*(E5), 2007JE002984. https://doi.org/10.1029/2007JE002984

Kremer, C. H., Mustard, J. F., & Pieters, C. M. (2020). Cross-Over Infrared Spectroscopy: A New Tool for the Remote Determination of Olivine Composition. *Geophysical Research Letters*, *47*(20), e2020GL089151. https://doi.org/10.1029/2020GL089151

Kremer, C. H., Mustard, John. F., & Pieters, C. M. (2023). Intermediate Infrared Spectroscopy of Pyroxene: Determination of Ca-Mg-Fe Composition in the 4–8 Micron Wavelength Range. *Earth and Space Science, 10*(5), e2023EA002828. https://doi.org/10.1029/2023EA002828

Kremer, C. H., Mustard, J. F., Pieters, C. M., Gillis-Davis, J. J., & Donaldson Hanna, K. L. (2022). Spectral effects of nano-phase iron and agglutinates in olivine, plagioclase, and lunar soils in the "cross-over" infrared range (4-8 microns). *Presented at the Lunar and Planetary Science Conference LIII*, (p. 2239).

Lane, M. D., Glotch, T. D., Dyar, M. D., Pieters, C. M., Klima, R., Hiroi, T., et al. (2011). Midinfrared spectroscopy of synthetic olivines: Thermal emission, specular and diffuse reflectance, and attenuated total reflectance studies of forsterite to fayalite. *Journal of Geophysical Research*, *116*(E8), E08010. https://doi.org/10.1029/2010JE003588

McCord, T. B., & Clark, R. N. (1979). The Mercury soil: Presence of Fe^{2+}. *Journal of Geophysical Research: Solid Earth*, *84*(B13), 7664–7668. https://doi.org/10.1029/JB084iB13p07664

Milliken, R. E., & Mustard, J. F. (2005). Quantifying absolute water content of minerals using near-infrared reflectance spectroscopy. *Journal of Geophysical Research: Planets*, *110*(E12), 2005JE002534. https://doi.org/10.1029/2005JE002534

Nittler, L. R., Starr, R. D., Weider, S. Z., McCoy, T. J., Boynton, W. V., Ebel, D. S., et al. (2011). The Major-Element Composition of Mercury's Surface from MESSENGER X-ray Spectrometry. *Science*, *333*(6051), 1847–1850. https://doi.org/10.1126/science.1211567

Pérez-López, S., Kremer, C., & Mustard, J. (2023). Dataset and code for 'Signal to Noise Ratio and Spectral Sampling Constraints on Olivine Detection and Compositional Determination in the Intermediate Infrared Region' [Data set]. Zenodo. https://doi.org/10.5281/zenodo.10368444

Shearer, C. K., Elardo, S. M., Petro, N. E., Borg, L. E., & McCubbin, F. M. (2015). Origin of the lunar highlands Mg-suite: An integrated petrology, geochemistry, chronology, and remote sensing perspective. *American Mineralogist*, *100*(1), 294–325. https://doi.org/10.2138/am-2015-4817

Stutzki, J. (2006). SOFIA: The Stratospheric Observatory for Infrared Astronomy. In S. Röser (Ed.), *Reviews in Modern Astronomy* (1st ed., pp. 293–314). Wiley. https://doi.org/10.1002/9783527619030.ch14

Sunshine, J. M., Pieters, C. M., & Pratt, S. F. (1990). Deconvolution of mineral absorption bands: An improved approach. *Journal of Geophysical Research: Solid Earth*, *95*(B5), 6955–6966. https://doi.org/10.1029/JB095iB05p06955

Swayze, G. A., Clark, R. N., Goetz, A. F. H., Chrien, T. G., & Gorelick, N. S. (2003). Effects of spectrometer band pass, sampling, and signal-to-noise ratio on spectral identification using the Tetracorder algorithm. *Journal of Geophysical Research: Planets*, *108*(E9), 2002JE001975. https://doi.org/10.1029/2002JE001975

Ting, D. Z., Soibel, A., Hill, C. J., Keo, S. A., Mumolo, J. M., & Gunapala, S. D. (2012). High operating temperature midwave quantum dot barrier infrared detector (QD-BIRD). In B. F. Andresen, G. F. Fulop, & P. R. Norton (Eds.) (pp. 835332-835332–8). Baltimore, Maryland. https://doi.org/10.1117/12.920685

Wood, J. A., Dickey, J. S., Marvin, U. B., & Powell, B. N. (1970). Lunar Anorthosites. *Science*, *167*(3918), 602–604. https://doi.org/10.1126/science.167.3918.602

Supplementary Figures

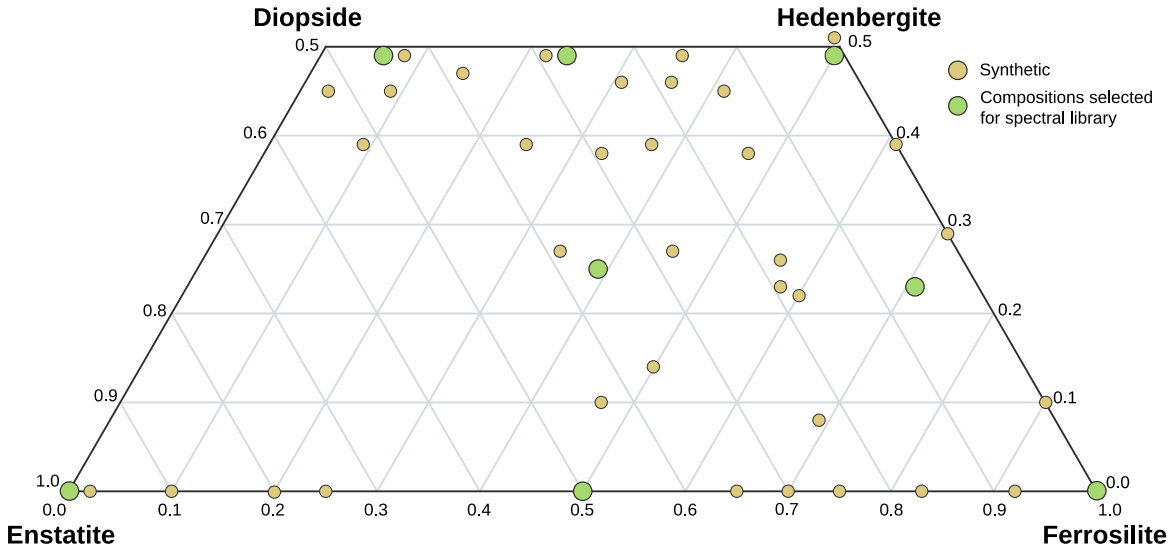

Figure S1. Synthetic pyroxene suite synthesized by Donald Lindsley (beige markers) and compositionally representative selection of samples that are included in spectral library (green markers).

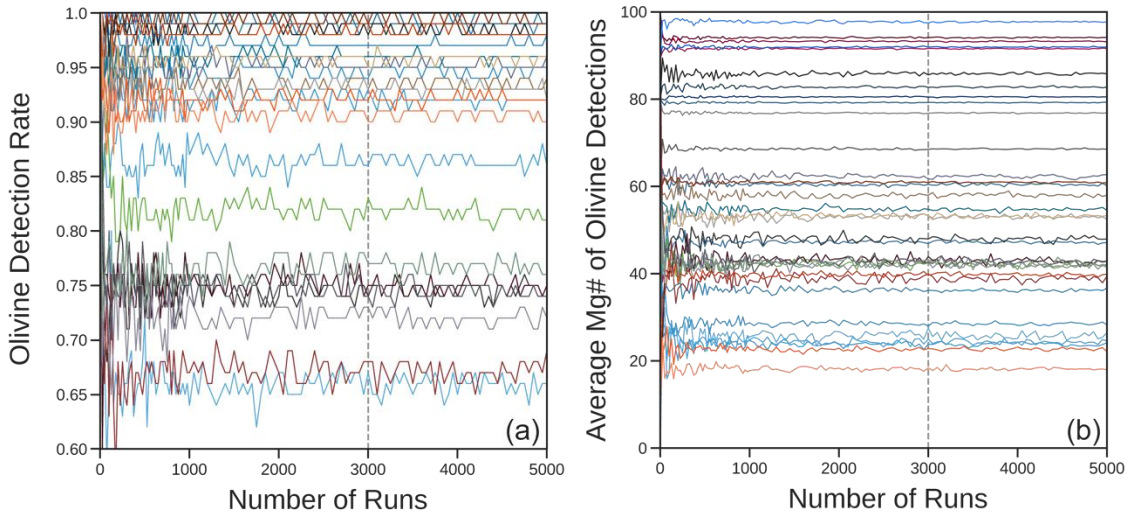

Figure S2. a) Olivine detection rate and b) average Mg# of olivine detections for all test spectra across and increasing number of runs. Raw data.

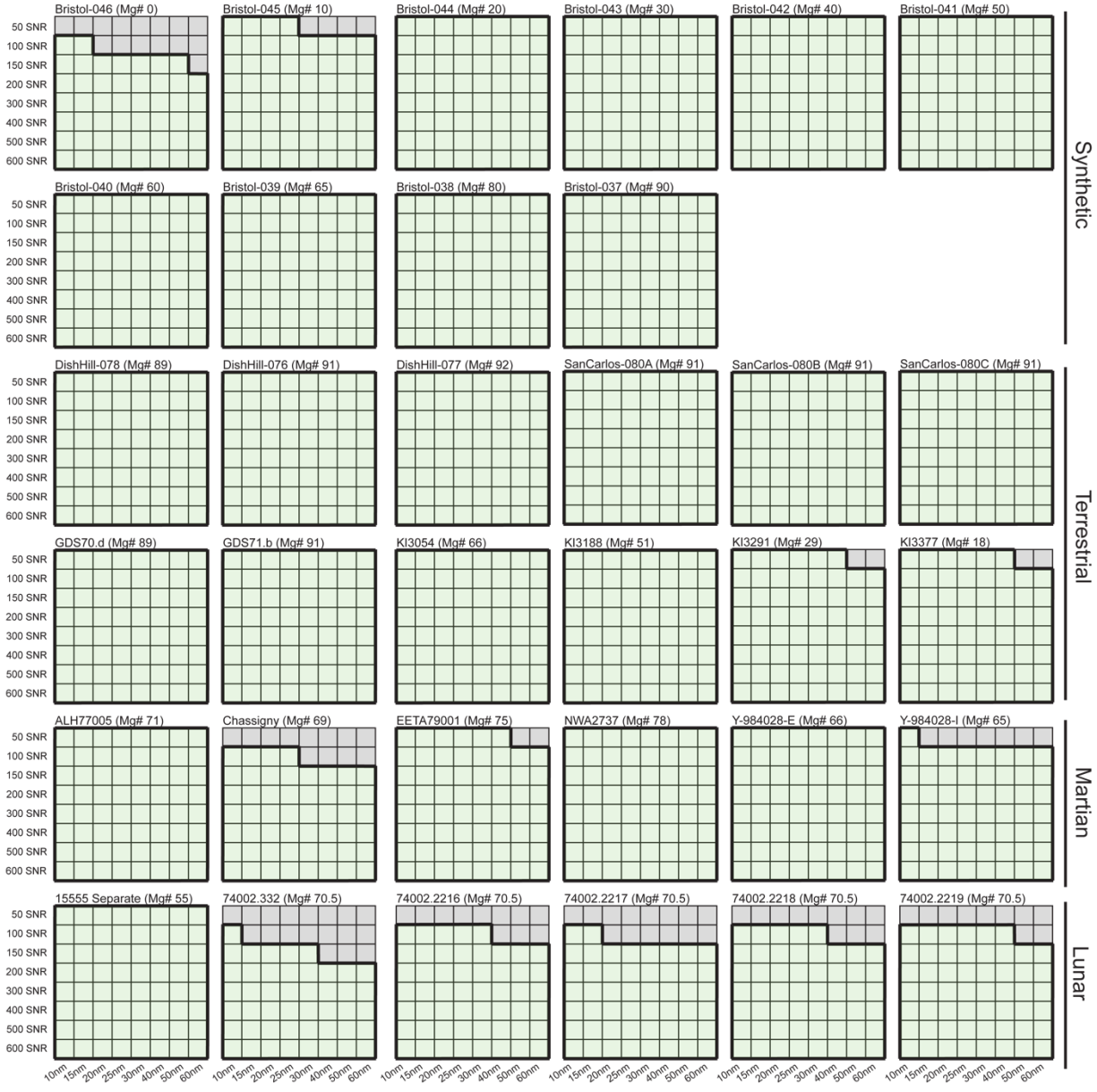

Figure S3. Parameter space required to achieve 100% olivine detection across 3000 runs for all test spectra. Green grid space denotes data qualities (SNR and sampling rate) where 100% olivine detection was achieved, gray grid spaces denote data qualities where 100% olivine detection was not achieved. Each grid space represents the result of 3000 feature fits, with each iterations generating a new degraded test spectra with randomly sampled noise defined by that grid's SNR and resampled to the grid's sampling rate.

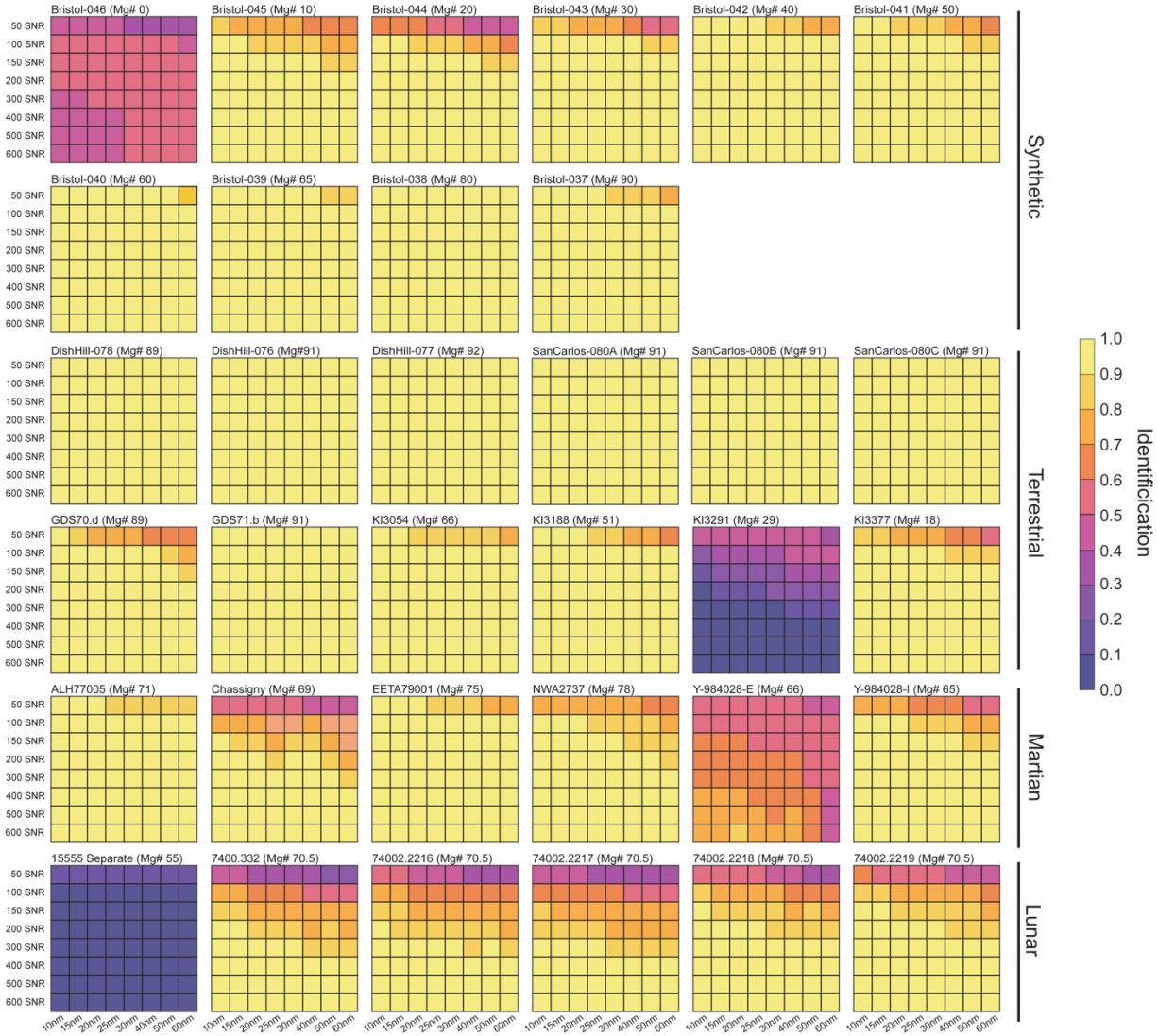

Figure S4. Identification rates within ±12 Mg# of test spectrum's true composition across a set of feature fitting runs for all data qualities explored in this study. Each grid space represents the result of 3000 feature fits, with each iterations generating a new degraded test spectra with randomly sampled noise defined by that grid's SNR and resampled to the grid's sampling rate.